*Egypt. J. Chem.* **Vol. 66**, No. 7 pp. 345 - 359 (2023)

**Egyptian Journal of Chemistry**

**http://ejchem.journals.ekb.eg/**

# Facile Synthesis and Properties of Cu-Based Supported Halloysite Nanotube (HNT) Photocatalysts for Photocatalytic Degradation of Liquid Epoxidized Natural Rubber (LENR)

**Shehu Sa'ad Abdullahi [1,2], Noor Hana Hanif Abu Bakar [1]*, Anwar Iqbal [1], Nurul Hayati Yusof [3]**

[1]*Nanoscience Research Laboratory, School of Chemical Sciences, Universiti Sains Malaysia, Penang, 11800, Malaysia*

[2]*Department of Polymer Technology, Hussaini Adamu Federal Polytechnic Kazaure, Jigawa, P.M.B.5004, Nigeria*

[3]*Malaysian Rubber Board, Engineering and Technology Division, Sungai Buluh, Selangor, 47000, Malaysia*

**Abstract**

$Cu^{2+}$-HNT nanocomposite was synthesized via impregnation of $CuSO_4.5H_2O$ onto halloysite nanotube (HNT). A portion of the nanocomposite was calcined at 550 and 900 °C respectively, to obtain CuO-HNT catalysts. The FTIR, XRD and EDX results reveals the successful formation of nanocomposites. This is consistent with the decrease in the nanocomposite $S_{BET}$ and pore volume for $Cu^{2+}$-HNT, and CuO-HNT calcined at 550 and 900 °C, respectively, when compared to HNT. Optical properties of both the HNT, and nanocomposites show a decrease in the bandgaps of the nanocomposites. The GPC results of pristine LENR (P-LENR) and photo-degraded LENR showed that LENR treated with calcined CuO-HNT at 550 °C gives lowest LENR molecular weight of 3,105 g/mol compared to 25,732 g/mol of P-LENR with 88 % degradation within 3 hours UV-irradiation. Changes in the functional group of degraded LENR was observed.

***Keywords:*** Calcined; CuO; HNT; LENR; Photodegradation

## 1. Introduction

The current method in producing energy and fine chemicals using fossil fuels has led to global warming and climate change [1]. Over the last few decades, scientists have focused on renewable resources as an alternative method to produce energy and fine chemicals [2]. Biomass has now gained the attention of many researchers because of its availability. The utilization of forestry residues and products, are being developed to convert biomass to valuable products [3]. In previous studies, several attempts have been made to depolymerize biomass via liquefaction [4], hydrothermal carbonization [5], gasification [6], pyrolysis [7], hydrogenolysis [8] and catalytic oxidation [3]. The major limitations of these methods are side reactions, excess use of solvents, high pressure, and temperature[9,10]. Hardly any work has employed photocatalytic degradation, even though this method can be considered as a sustainable method. Mostly, photocatalytic degradation has been used to eliminate harmful organic substances discharged into the environment [4,11].

Photocatalytic degradation is more effective when metal-based catalyst is used in the reaction [11]. Transition metals have been known to possess outstanding catalytic activity for degrading organic substances because of their high surface area (when in nanosize), and electron-holes formation [12,13]. The use of various supports for transition metal catalyst improve their catalytic efficiency compared to unsupported catalyst due to the increase in catalyst active phase dispersion [5]. When nanoparticles are distributed on large-surface-area supports, their interactions with the support can improve catalytic efficiency [14]. Numerous supports such as carbon

*Corresponding author e-mail: hana_hanif@usm.my (N.H.H Abu Bakar)
EJCHEM use only: Received date 11 May 2022; revised date 29 August 2022; accepted date 06 October 2022
DOI: 10.21608/EJCHEM.2022.136214.6070

nanotubes, zeolite, dendrimers [15], titanium dioxide, alumina and silica have been used for metal nanoparticles [16]. It has been reported that degradation efficiency increases when transition metals are supported on carbon nanotubes [9]. However, carbon nanotubes and zeolite have complex preparation methods and can be expensive to prepare. Furthermore, the structure of carbon nanotubes can disintegrate at higher temperature, and this can result in small surface area [17]. In contrast, clays such as montmorillonite (lamellar), sepiolite (fibrous), kaolinite (lamellar), and halloysite nanotubes (HNT) (tubular), occur naturally in a variety of shapes and sizes [18]. Clays have been used as metal catalyst supports because it is stable at high temperature, high surface area, less expensive, eco-friendly, resistance against organic solvent and availability [14]. HNT is a particularly interesting nanomaterial because of its diverse features, including hollow tube shape, high specific area, and changeable surface chemistry [19]. HNT can be utilised as a support for metal nanoparticles. Zhang et al., reported the incorporation of metals such as (Co and Pd) on HNT to yield nanocomposites which showed high catalytic activity in the hydrogenation of styrene to ethylbenzene within 30 minutes [20]. Moreover, incorporating metal oxides with clay to yield a clay-semiconductor nanocomposite has excellent catalytic efficiency compared to the unsupported catalyst [21]. Carrillo & Carriazo [22] conducted research on the preparation of CuO and CoO supported HNT and determined its catalytic activity. The results indicates that the catalysts have high catalytic performance for the degradation of several environmental pollutants like toluene and benzyl alcohol, respectively [23]. Cu-based catalysts are p-type semiconductors with an excellent UV-absorption ability [19].

Epoxidized natural rubber (ENR) is a derivative of natural rubber (NR). It is formed via the introduction of epoxy linkage on NR. ENR comprises of shorter polymeric chains compared to the conventional NR, with part of the C=C being changed into the epoxy group [24]. Liquid epoxidized natural rubber (LENR) is the derivative of ENR which is obtained from the degradation of ENR, typically, through mechanical grinding, chemical degradation in the presence of potassium peroxydisulfate, and photooxidation initiated by ultraviolet irradiation [25]. UV degradation method resulted in a higher LENR yield within shorter reaction time when compared with mechanical grinding and chemical degradation methods. The amount of ENR molecular weight degradation recorded within 4 hours reaction time using UV-photodegradation method was found to be more than the one obtained using both mechanical grinding (after 8 hours) and chemical degradation methods (after 15 hours) [25]. The preparation of LENR via UV irradiation is less costly and can produce chemical intermediates such as hydro furan in addition to ketones, aldehydes, carboxylic acid, ester and lactone which are used in industry [25]. In a separate study, Rooshenass et al. [26], reported the preparation of LENR by oxidative degradations using periodic acid, potassium permanganate and UV-irradiation. They were able to study ENR oxidative degradation by using both periodic acid, potassium permanganate and UV irradiation. All three methods show certain degree of degradation, but periodic acid was found to have the lowest Mn and fastest degradation rate.

To date, very few works has used a catalyst in the presence of UV irradiation to degrade natural polymers. No work has reported on the use of metal-based catalysts in the presence of UV light to degrade LENR. It has been reported that catalysts such as zirconia and titania-based metal oxides can be used for the catalytic pyrolysis of pine wood. They were found to demonstrate high bio-oil yield [27]. Ibrahim et al. [28], studied the functionalization of liquid natural rubber (LNR) via oxidative degradation of NR with the aid of hydrogen peroxide and sodium nitrite as reagents leading to the formation of LNR by chemical degradation technique. On the other hand, Bahruddin et al. [29], studied the molecular weight of LNR product from the chemical depolymerization process of high molecular weight NR latex. The depolymerization was carried out in the presence of $NaNO_2$, $H_2O_2$ as degrading agents and $CoCl_2$ as catalyst at 80 °C temperature. The result showed a decrease in molecular weight from 1,384,638 g/mol to 108,335 g/mol. Ibrahim et al. [30], conducted research on the preparation and characterization of low-molecular-weight NR latex via photodegradation catalyzed by nano $TiO_2$. The use of $TiO_2$ as a catalyst enhanced the photodegradation efficiency of NR leading to drastic decrease of the molecular weight from $549.3\times10^3$ g/mol to $7.3\times10^3$ g/mol.

Research on the depolymerization of biopolymers using metal-based nanoparticles as active phase on HNT is limited in literature. Although the synthesis on CuO on HNT has been studied before, the synthesis procedures differed based on the different potential applications [31]. As an example, Cavallaro and coworkers [19]. prepared CuO-HNT by modifying the HNT so that it exhibits both hydrophilic and hydrophobic properties. This enabled its use for antibacterial purposes. To date, no research

has been conducted on the degradation of LENR using Cu-based photocatalyst supported HNT via UV exposure technique. The Cu-based catalyst was chosen in this study due to its readily availability and low cost. Therefore, this work, aims to prepare and characterize several $Cu^{+}$-HNT and CuO-HNT photocatalysts for the degradation of LENR with the aid of the UV exposure method. As per literature survey, this is the first report on a greener method for the degradation of LENR.

## 2. Experimental

### 2.1 Materials

LENR with 50% of epoxidation was obtained as a gift from the Malaysian Rubber Board, Halloysite nanotube (HNT) was purchased from Sigma Aldrich, USA, and was used as received. Copper sulfate ($CuSO_4.5H_2O$) with a purity of 99% was purchased from Fluka, Switzerland, All the reagents used are of analytical grade.

### 2.2 Catalyst Preparation

The $Cu^{2+}$-HNT catalyst was prepared similarly to the procedure reported by [32], however with some modifications. In a typical synthesis, 0.5 M of $CuSO_4.5H_2O$ was prepared by dissolving 1.2484 g of $CuSO_4.5H_2O$ in 10 ml distilled water. As much as 7.18 mL of 0.5 M $CuSO_4.5H_2O$ solution was added to 5 g of HNT for the preparation of 4.6 wt % of Cu in HNT. The solution was stirred for 24 h to form $Cu^{2+}$-HNT. Thereafter, the resulting catalyst was filtered and oven-dried at 60 °C for 6 hours. $Cu^{2+}$-HNT were then stored in a desiccator for further characterizations.

A portion of the resulting catalyst was placed in a furnace and calcined at different temperatures of 550 and 900 °C for 3 h respectively [33]. After cooling, the calcined and un-calcined catalyst were taken for analysis.

### 2.3 Characterization Techniques

The crystallinity of the samples was acquired using a Philips X'pert Pro X-ray diffractometer (PW 3040 model) (Frimly UK). A Cu-Kα radiation source (λ = 1.54 Å) at 40 kV and 40 mA current with a continuous sweep in the 2θ range of 10 to 90°, scan at a rate of 0.02° $s^{-1}$ was used. The surface morphologies and elemental dispersions of the HNT, as-synthesized $Cu^{2+}$-HNT, and CuO-HNT calcined at 550 and 900 °C nanoparticles were acquired using a FEI Quanta FEG 650 scanning electron microscope (SEM) (Holland) equipped with energy-dispersive X-ray spectroscopy (EDX). The samples were sputter-coated with platinum before the analysis. The surface area and porosity of HNT, as-synthesized $Cu^{2+}$-HNT, and calcined CuO-HNT at 550 and 900 °C catalysts, were obtained via $N_2$ adsorption-desorption using Brunauer-Emmett-Teller (BET) and Barrett-Joyner-Halenda (BJH) techniques (Quanta chrome, Boynton Beach, FL, USA). The samples specific surface areas were acquired from the BET method whereas the pore size and volumes were measured from the curves of the desorption isotherm via the BJH method. Perkin Elmer Lambda LS 35 UV/Vis spectrometer (Singapore) was used to determine the UV-Vis diffusion reflectance and absorbance spectra of the HNT, and as-synthesized catalysts in the region of 200-800 nm. While the fluorescence of the HNT and as-synthesized catalysts were acquired using Fluorescence spectrometer Perkin Elmer LS55 (Singapore). Samples were analyzed using Attenuated total reflectance-Fourier-transform infrared (ATR-FTIR Microscope Spotlight 200 ATR (Direct-Q 8 UV-R) Billerica, (USA) spectroscopy. The spectra of HNT, as-synthesized calcined, un-calcined catalyst, P-LENR, photodegraded LENR with and without catalyst were acquired within the frequency range of 4000-600 $cm^{-1}$ at room temperature. The thermal stability of P-LENR and degraded LENR was determine using TGA technique. The P-LENR and degraded LENR was thermally decomposed from 30 to 900°C in a nitrogen atmosphere using a TGA/SDTA 851 Mettler Toledo (USA) instrument at a heating rate of 20 °C $min^{-1}$. For atomic adsorption spectroscopy (AAS) analysis, the nanocomposites were digested using a modified procedure [34]. As much as, 0.1 g of the dried nanocomposite sample was digested with 6 $cm^3$ of concentrated $HNO_3$ and 2 $cm^3$ of concentrated HCl in crucible vessels. After digestion, the sample was transferred into the 100 $cm^3$ volumetric flask, filled to the mark with ultra-pure water and the solution was filtered and kept in polyethylene (PE) sample bottles for AAS analysis. The sample was later analyzed using AAS technique to determine Cu content. An Analyst 400, Perkin Elmer was used to determine the Cu content of the composite samples. The weight average molecular weight, $M_w$ and number average molecular weight, $M_n$ for P-LENR and degraded LENR were measured with a GPC (TOSOH HLC-8320GPC) that consists of RI detector, and two columns (TSK gel Super Multipore HZ-M). The measurement was performed at 30 $^oC$ at a flowrate of 1 mL/min. The molecular weight was read against polystyrene calibration curve.

### 2.4 Catalytic studies

#### 2.4.1 Photocatalytic experiments

As much as 0.05g of calcined and un-calcined $Cu^{2+}$-HNT catalysts were mixed separately with 1 g LENR

and dissolved in 20 ml of toluene. The solution was stirred at room temperature and a 500-watt UV Zenon lamp was placed 15 cm above the solution for 3 hours with continuous stirring. The resulting mixture was centrifuged at 3500 rpm for 10 minutes to separate the catalyst from degraded LENR. For the latter, the solution was dried at 60 °C in an oven for 3 hours [35]. The samples were subjected for further analysis.

## 3. Results and Discussion

### 3.1. XRD analysis

Figure 1 depicts the XRD pattern of HNT, $Cu^{2+}$-HNT, CuO-HNT (calcined at 550 and 900 °C), in the 2θ range of 0-90°. In the XRD diffractogram shown in Fig. 1(a), the HNT exhibit reflections at 2θ values of 12.21° (001), 20.15°(100), 24.84°(002), 26.58°(003), 34.78°(110), 38.28°(200), 54.73°(210), 62.50°(300), 73.77°(220), 77.27°(310). These corresponds with the standard JCPDS Card number 09-0453 for HNT [36]. It has been established from literature that the peak at 26.58° is attributed to quartz ($SiO_2$) present in the HNT whereas the peak at 62.50° indicates the HNT with dioctahedral arrangement [32].

The XRD patterns of $Cu^{2+}$-HNT is shown in Figure 1(b) and compared to pristine HNT. Spectral peaks of the $Cu^{2+}$-HNT nanocomposite were found to have a similar pattern with pristine HNT. However, peaks at 2θ values of 12.33° (001), 20.15° (100) 38.28° (200) and 62.50° (113) were shifted to 12.58° (001), 20.23° (100) 39.72° (130), 62.70° (113) respectively. This implies the successful compositing of HNT with $Cu^{2+}$ salt. A new peak (denoted by *) at 2θ value of 33.77° (002) exist as a result of the presence of $CuSO_4$ and this agrees with findings of [32].

The XRD diffractogram of the calcined catalyst (CuO-HNT at 550 °C and 900 °C) as seen in Figure 1(c) and 1(d), shows similar peaks as the HNT as well as new diffraction peaks. The intensity of the peaks of HNT differs from pristine HNT. This is attributed to the calcination treatments as reported previously [37]. Most peaks decreased in intensity, however, the peak at 26.58° became broad and increased in intensity. The decrease in peak intensity can be because the HNT undergoes a certain degree of amorphization. Subsequently, the available XRD diffraction peaks indicate the formation of both CuO and $Cu_2O$ in the composite. The main peaks for CuO (denoted as @) are positioned at 35.5°, 38.6° and 53.8°. These peaks are attributed to the (002), (200) and (020) planes respectively. In contrast, the main peaks for $Cu_2O$ arise at 36.8° and 42.6° (denoted as #). These peaks correlate with the (111) and (200) planes of $Cu_2O$. The peak assignments correspond with the peaks reported elsewhere [38]. However, the peaks for both CuO and $Cu_2O$ are slightly shifted from their original values due to the presence of HNT.

The Debye–Scherrer formula (Equation (1)) was used to measure the average size of CuO and $Cu_2O$ particles in the CuO-HNT composites calcined at 550 and 900 °C. In contrast, the Bragg's Law (Equation (2)) was employed to determine the d-spacing of HNT in the pristine HNT as well as the composites.

$$D=K\lambda/B\cos\Theta \quad \ldots\ldots (1)$$

$$d=\lambda/2\sin\Theta \quad \ldots\ldots (2)$$

where, D = particle size, K = Scherrer constant, λ = X-ray wavelength, β = full width at half-maximum (FWHM) and θ = Bragg angle [39].

The average particles size of CuO and $Cu_2O$ formed in the nanocomposites calcined at 550 and 900 °C was calculated using the major diffraction peaks, namely (002), (200) and (020) for CuO and (111) and (200) planes of $Cu_2O$. The samples had CuO and $Cu_2O$ average crystallite sizes of 39.87 and 37.45 nm, as well as 37.28 and 32.75 nm for calcined nanocomposites at 550 and 900 °C respectively. The average basal d-spacing of the samples were calculated from the (001) diffraction plane at 2θ of approximately 12.21°. For HNT, a basal d-spacing value of 0.720 nm was obtained. But the d-spacing of uncalcined $Cu^{2+}$-HNT and calcined nanocomposites at 550 and 900°C CuO-HNT nanocomposites was found to slightly decrease to 0.694 nm (2θ = 12.38), 0.684 nm (2θ = 12.73), and 0.700 nm (2θ = 12.89) respectively. This indicates that the Cu based particles are physically incorporated on to the HNT surface and is not intercalated into the interlayer spacing of HNT.

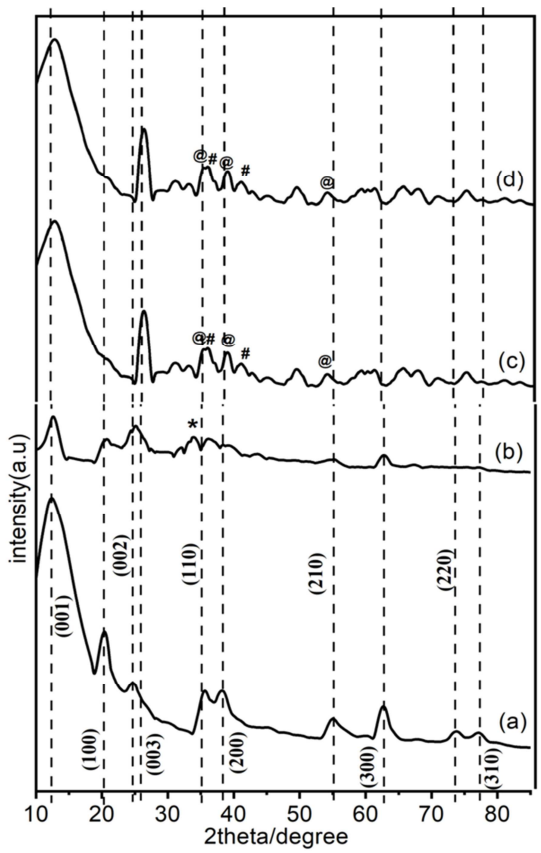


**Fig. 1:** XRD Spectra of (a) HNT (b) $Cu^{2+}$-HNT (c) Calcined CuO-HNT at 550 °C (d) Calcined CuO-HNT at 900 °C

### 3.2 FT-IR spectra of HNT and nanocomposites

Figure 2 shows the FTIR spectra of HNT, $Cu^{2+}$-HNT, and calcined CuO-HNT catalysts at 550 and 900 °C, respectively. As can be seen in Figure 2(a) The peaks at 3695 and 3618 $cm^{-1}$ are assigned to O-H stretching vibration which is attributed to inner-surface and inter-layer hydroxyl groups of HNT respectively [40]. While the peak at 1649 $cm^{-1}$ is related to the O-H vibration of adsorbed water on the HNT surface [41]. The peak at 1021 $cm^{-1}$ is due to the stretching vibrations of Si-O-Si [42]. In addition, the peak at 910 is attributed to vibration deformation of the inner hydroxyl group (O-H). The peak at 756 and 680 $cm^{-1}$ are assigned to the stretching vibrations of Si-O [14]. Figure 2(b) has a similar spectra peak compared to that of HNT except some peaks shifted to lower wavenumbers as in (1021-998 $cm^{-1}$, 910-902 $cm^{-1}$). The peak shift indicates a slight surface change in the HNT structure after metal salt impregnation which was reported in the literature by [43]. The peaks at 3410 and 1322 $cm^{-1}$ are attributed to the hydroxyl group vibration and bending due to adsorbed water on the catalyst surface [44]. The peak at 1406 $cm^{-1}$ is ascribed to the absorbed $CO_2$ from the air [45].

Figure 2(c) and 2(d) show the FTIR spectra of calcined CuO-HNT at 550 and 900 °C, respectively. They have similar peaks with the un-calcined $Cu^{2+}$-HNT catalyst, but some absorption peaks disappeared after calcination, particularly peaks in the region of 4000-3500 $cm^{-1}$, for the catalyst calcined at 900 °C [41]. This might be attributed to the loss of O-H groups from the Al-OH present in the HNT. This finding agrees with the literature reported by [46], that all impurities on HNT decompose when subjected to calcination at high temperature.

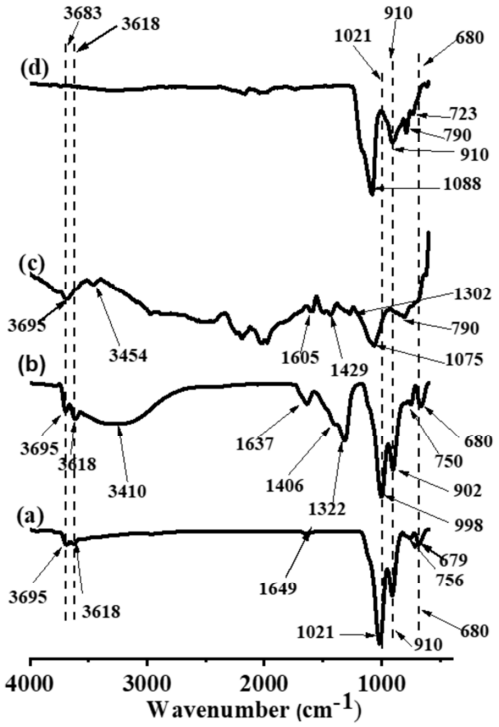


**Fig. 2:** FT-IR spectra of (a) HNT, (b) $Cu^{2+}$-HNT, (c) calcinated CuO-HNT at 550 °C, (d) calcinated CuO-HNT at 900 °C

### 3.3 AAS results

AAS was used to determine the Cu content of the composite samples. The amount of Cu present in the uncalcined and calcined nanocomposite samples were determined using AAS. The result showed the presence of Cu in the uncalcined $Cu^{2+}$-HNT, calcined at 550 and 900 °C CuO-HNT nanocomposites as 4.25, 4.20, and 4.16 wt % Cu, respectively.

### 3.4 FE-SEM images and EDX analysis

Figure 3 shows the SEM images of the HNT, $Cu^{2+}$-HNT, and CuO-HNT nanocomposites calcined at 550 and 900 °C, respectively. Only nanotubes exist in the image Figure 3(a) of the HNT. No individual particles are found on the outer region of HNT, as can be seen in the SEM image. Upon incorporation of $CuSO_4$ into the HNT, it can be seen that some aggregations exist on the surface of the HNT. These aggregations can be due to the presence of copper salt as can be seen in Figure 3(b). This is supported by the EDX analysis of the sample which shows the presence of sulfur (Figure 4). Upon calcination of the $Cu^{2+}$-HNT at 550 °C, the CuO-HNT sample showed hardly any agglomerations were available compared to uncalcined $Cu^{2+}$-HNT as presented in Figure 3(c). No particles on the surface of HNT is seen on the surface. But smaller particles with some degree of agglomerations was observed on CuO-HNT sample calcined at 900 °C, as can be seen in Figure 3(d). These nanoparticles could have formed as a result of the sintering effect at high temperatures [46]. This reveals total combustion of carbon-based materials leaving behind CuO and HNT on the nanocomposite. The mean average particles size of the CuO in the nanocomposites sample calcined at 900 °C was calculated using imageJ plot and was found to be 36.7±2.1 nm. It clearly agrees with the particles size calculated from XRD diffractogram using Scherrer formula. However, the average particles size of the nanocomposites calcined at 550 °C was not determined. This is because there were no individual CuO particles on the surface of the nanocomposites as can be seen in Figure 3(c).

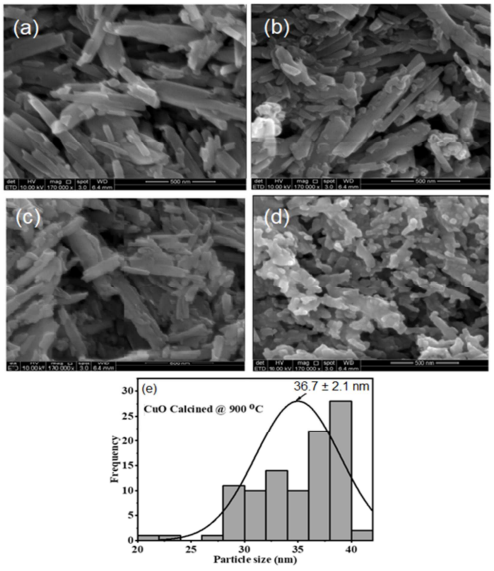


**Fig. 3:** SEM image of (a) HNT, (b) $Cu^{2+}$-HNT, (c) calcined CuO-HNT at 550 °C (d) calcined CuO-HNT at 900 °C

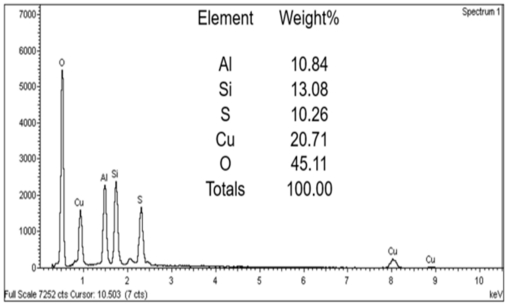


**Fig. 4:** EDX image of uncalcined $Cu^{2+}$-HNT

### 3.5 BET analysis

The surface area ($S_{BET}$), pore size, and pore-volume of HNT, $Cu^{2+}$-HNT, CuO-HNT calcined at 550 °C and 900 °C nanocomposites were determined via $N_2$ adsorption desorption technique and presented in Table 1. The respective $N_2$ adsorption-desorption isotherm and pore size distribution (BJH) curve is presented in Figure 5(a-d). HNT has a BET surface area ($S_{BET}$) of 52.21 $m^2/g$ and pore volume of 0.22 $cm^3/g$ respectively. The $S_{BET}$ and pore volume of the nanocomposites were found to be lower than that of pristine HNT after incorporation with $CuSO_4$. The $Cu^{2+}$-HNT $S_{BET}$ and pore volume values are 37.23 $m^2/g$ and 0.13 $cm^3/g$ respectively. A portion of $Cu^{2+}$-HNT nanocomposite was subjected to calcination at 550, and 900 °C to produce calcined CuO-HNT. A decrease in the nanocomposites $S_{BET}$ and pore volume was observed (35.87 $m^2/g$, 0.13 $cm^3/g$) and

(9.27 $m^2/g$, 0.064 $cm^3/g$) respectively. The decrease in the $S_{BET}$ and pore volume of the calcined nanocomposite at 550 °C compared to the un-calcined $Cu^{2+}$-HNT maybe a result of the CuO nanoparticles formed at 550 °C occupying the HNT nanotubes [47]. In contrast, the drastic decrease in $S_{BET}$ and pore volume of the nanocomposite calcined at 900 °C, might also be due to the distortion of the crystalline lattice of the nanocomposite material when the calcination temperature is above 600 °C as reported by [17]. Subsequently, the pore size diameter also showed a decreasing trend especially for the sample calcined at 900 °C. This is consistent with the formation of agglomerated CuO nanoparticles formed blocking the pores as well as the possible distortion of the crystalline lattice. SEM images support this finding. The isotherm shows a type IV pattern with a H3 hysteresis loop, indicating that the catalysts produce mesopores (according to IUPAC classification) at a relative pressure of 0.4 to 1.0. This is attributed to the wide size range of mesopores and macropores. The type of isotherms did not change, and the pore structure is preserved after impregnation of $Cu^{2+}$ salt onto HNT and subsequent calcinations, as observed in the Figure 5(b-d). A similar observation was reported by several researches as presented in Table 1.

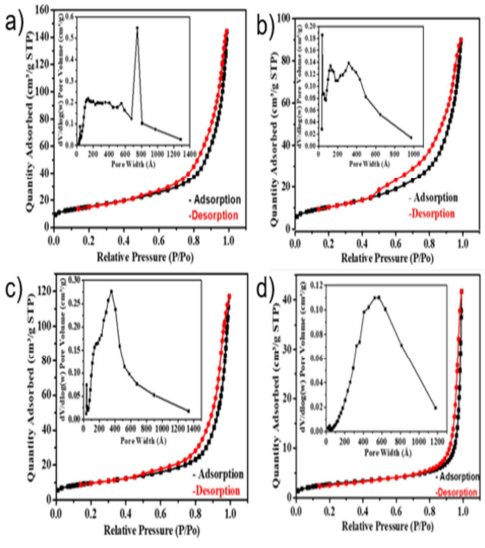


**Fig. 5:** Typical $N_2$ adsorption-desorption isotherms for (a) HNT (b) $Cu^{2+}$-HNT, (c) calcined CuO-HNT at 550 °C (d) calcined CuO-HNT at 900 °C [Inset: BJH pore size distribution plot]

**Table 1**
Comparison of surface properties of various Cu based HNT composites

| Samples | $S_{BET}$ ($m^2/g$) | Average pore diameter (nm) | Pore volume ($cm^3/g$) | Ref. |
|---|---|---|---|---|
| HNT | 59.12 | 266.78 | 0.31 | [47] |
| | 45 | 27 | 0.26 | [48] |
| | 52.21 | 174 | 0.22 | Present study |
| $Cu^{2+}$-HNT | 35.90 | 16.14 | 0.16 | [32] |
| | 37.23 | 15.37 | 0.13 | Present study |
| CuO-HNT calcined (550 °C) | 28.00 | 15 | 0.13 | [48] |
| | 35.90 | 209.57 | 0.25 | [47] |
| | 35.87 | 14.49 | 0.13 | Present study |
| CuO-HNT calcined (900 °C) | 9.27 | 3.74 | 0.064 | Present study |

### 3.6 Optical Properties

Figure 6 (i) shows the UV-Vis spectra of HNT, $Cu^{2+}$-HNT, and calcined CuO-HNT at 550 and 900 °C, respectively. As can be seen in Figure 6(i) the absorbance peaks of HNT are located at 212 and 257 nm. Previous work has reported that clays often give rise to two peaks in the UV region. In clays, these peaks are commonly due to the presence of traces of oxo-iron (iii) octahydrates [49]. However, as iron is not present in HNT (based on EDX), the appearance of these peaks are not fully understood. Another work has reported that the presence of -OH functional groups on HNT can cause the intensity in this region to increase. However only broad peaks were observed by [50]. In contrast, $Cu^{2+}$-HNT, as well as calcined CuO-HNT at 550 and 900 °C have peaks located at 247, 234, and 241 nm, respectively. Previous research has shown that the absorbance peak for CuO is found to be around 250- 255 nm [51]. In this work, the peak for the catalyst is slightly shifted to a lower absorption peak which might be due to the formation of Cu-based nanocomposites with HNT.

Direct band gap occurs when the maximum energy

level of valence band aligns with the minimum energy level of the conduction band with respect to momentum. Direct recombination can take place. The probability of radiative recombination is very high, and its efficiency factor is very high. while indirect band gap occurs when the maximum energy level of the valence band and minimum energy level of conduction band are not aligned with respect to momentum. The probability of radiative recombination is almost negligible and efficiency factor is very low.

The energy bandgap of the samples was determined using Tauc's relation [52].

$$(\alpha h\nu)^n = A(h\nu - Eg) \ldots\ldots\ldots\ldots\ldots\ldots\ldots (3)$$

where α = absorption coefficient, hν = photon energy, A = absorbance, Eg = optical bandgap, n = number describing the nature of the transition process; n = 2 for the direct transition and n =1/2 for an indirect transition. Hence, the optical bandgap for the absorption edge can be obtained by extrapolating the linear portion of the $(\alpha h\nu)^{1/2}$ against hν curve to the energy on the X-axis [52]. The band gaps of the HNT and as-synthesized catalyst were obtained using Tauc's plot as presented in figure 6(ii). It can be seen from the bandgap's plots of all the as-synthesized catalysts were within the visible light region. Moreover, the bandgap of the pristine HNT which is 3.54 eV is higher compared to the calcined and un-calcined catalysts. It is observed that the catalysts band gap decreases after calcination of $Cu^{2+}$-HNT. The value shifted from 3.39 eV for $Cu^{2+}$-HNT to 2.51 eV for CuO-HNT calcined at 500 ºC and 3.11 eV for CuO-HNT calcined at 900 °C. The difference in the bandgap of the calcined CuO-HNT at 500 °C and 900 °C maybe attributed to the difference in size of the CuO particles as a result of the variation in calcination temperature. Similar observations have been reported elsewhere [53]. This is probably due to decomposition of organic materials present in the HNT and formation of CuO semiconductor in the nanocomposites.

$$Eg = hc/\lambda \ldots\ldots\ldots\ldots\ldots\ldots\ldots\ldots\ldots\ldots (4)$$

Photoluminescence of HNT and the Cu based catalysts was determined at room temperature. As presented in Figure 6(iii), at an excitation wavelength of 200 nm, HNT gave rise to a strong PL emission peak at 347 nm and a weak PL emission peak at 696 nm. At the same excitation wavelength, $Cu^{2+}$-HNT nanocomposites show a similar strong PL emission peak at 326 and 648 nm which might be attributed to the formation of nanocomposite which results in the decrease in the PL emission peaks in comparison with that of HNT. This agrees with the literature reported by [54]. However, when the same excitation wavelength was used for CuO-HNT calcined at 550 °C strong PL emission peaks was observed at 321 and 641 nm and small PL emission peaks was seen at 444 nm, respectively this corresponds to findings of [55]. But the PL strong emission peaks for CuO-HNT calcined at 900 °C at 200 nm excitation wavelength were found to be at 349 and 699 nm. A decrease in the emission wavelength was observed for both $Cu^{2+}$-HNT and CuO-HNT calcined at 550 °C. This might be due to the presence of $Cu(OH)_2$ or CuO in the nanocomposite. However, almost similar emission peak with HNT was noticed for the CuO-HNT nanocomposite calcined at 900 °C because the strong emission peaks was observed at 347 nm and small emission peak at 697 nm. As can be seen the emission peaks of calcined CuO-HNT at 900 °C is nearly similar with the pristine HNT. This might be attributed to the higher calcination temperature used which results in the distortion of crystallinity of the nanocomposite. Generally a shift of the emission peaks of the nanocomposites to a lower wavelength compared to the pristine HNT was observed which results in decrease in the electron-hole recombination which leads to increase in nanocomposite photocatalytic efficiency [56].

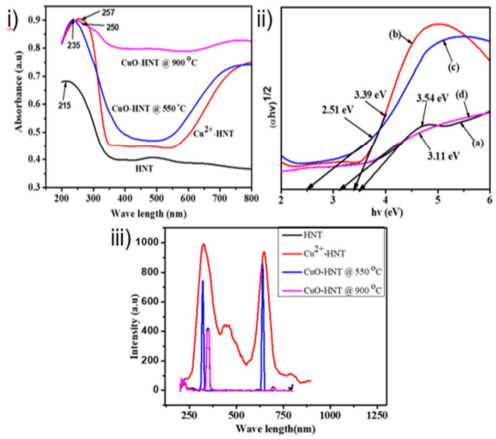


**Fig. 6:** (i) UV-Vis absorption spectra (ii) (a-d) band gap energies (iii) PL emission spectra with 1% attenuator of HNT, $Cu^{2+}$-HNT, Calcined CuO-HNT at 550 and 900 °C
[(a) HNT, (b) $Cu^{2+}$-HNT, (c) CuO-HNT calcined at 500 ºC and (d) CuO-HNT calcined at 900 ºC]

### 3.7 Photodegradation and Characterization of Degraded LENR

#### 3.7.1 Gel permeation chromatography (GPC)

GPC analysis was used to study the changes in molecular weight observed on LENR and its corresponding degraded derivatives. The results of weight average molecular weight ($M_w$), number average molecular weight ($M_n$), and polydispersity indexes of P-LENR and degraded LENR samples are presented in Table 2. The results revealed that the $M_w$ of all degraded LENR samples showed a significant decrease when compared with that of the P-LENR. This could be attributed to the degradation of LENR chain, which arises due to chain scission resulting in the formation of low $M_w$ compounds. The result indicated that the $M_w$ of LENR decreased from 25,732 to 12,067 g/mol after being subjected to UV-irradiation photodegradation for 3 hours in the absence of catalyst. However, when irradiated in the presence of $Cu^{2+}$-HNT catalyst, the $M_w$ further decreases from 25,732 to 5,774 g/mol. This might be due to dispersion of photocatalysts resulting in its good photocatalytic activity on LENR. When the CuO-HNT calcined at 550 °C was used, the $M_w$ dropped dramatically to 3,105 g/mol. This might be attributed to the different active sites available when $Cu^{2+}$ ions are oxidized to CuO. The low band gap energy observed by the CuO-HNT calcined at 550 ºC could also have contributed to the better photocatalytic degradation of LENR. Its lower band gap energy can be related to higher visible light harvesting ability. However, the $M_w$ of LENR degraded with UV-irradiation in the presence of CuO-HNT calcined at 900 °C reduces to only 8,078 g/mol. The degradation was less when compared to LENR treated with un-calcined catalyst. This may be attributed to the low surface area because of high calcination temperature of 900 °C for the nano-composites which eventually causes a high degree of agglomeration as such the active sites for the degradation decreases [57, 58]. The calcined catalyst at 550 °C was found to have the highest catalytic activity for the degradation of LENR compared to the remaining samples due to the formation of low $M_w$ of the degraded LENR. Generally, smaller particles have higher oxygen vacancy contents, which results in higher UV-vis absorption. Higher calcination temperatures resulted in the development of crystals, which reduced the optical activity of the resulting catalysts [59].

**Table 2**
$M_w$, $M_n$, and polydispersity indexes (PDI) of P-LENR and degraded LENR

| Samples | Weight average molecular weight ($M_w$) ($x10^3$) g/mol | Number average molecular weight, ($M_n$) ($x10^3$) g/mol | Polydispersity index (PDI) ($M_w/M_n$) | Percentage degradation $\frac{Mw1 - Mw2}{Mw1} \times 100$ % |
|---|---|---|---|---|
| P- \LENR | 25.732 | 7.835 | 3.28 | - |
| LENR+ no catalyst | 12.067 | 2.095 | 5.76 | 53 |
| LENR+ 0.05g uncalcined $Cu^{2+}$-HNT | 5.774 | 1.381 | 4.18 | 78 |
| LENR+ 0.05g calcined CuO-HNT at 550 °C | 3.105 | 0.925 | 3.35 | 88 |
| LENR+ 0.05g calcined CuO-HNT at 900 °C | 8.078 | 1.595 | 5.06 | 69 |

#### 3.7.2 FT-IR spectrum of P-LENR and degraded LENR

FT-IR spectra of P-LENR, photodegraded LENR without catalyst, photodegraded LENR treated with 0.05g of $Cu^{2+}$-HNT and calcined CuO-HNT catalyst at 550 and 900 °C are shown in Figure 7(a-e) respectively. Figure 7(a) shows the FT-IR spectrum of P- LENR. The broad absorption peak located at 3423 $cm^{-1}$ is assigned to O-H stretching, while the peak at 2960 $cm^{-1}$ corresponds to C-H stretching vibration for the methyl group. The peaks located at 2925, 2870 $cm^{-1}$ are due to the stretching vibration of methylene. A small absorption peak was observed on P-LENR at around 1714 -1716 $cm^{-1}$ which is assigned to C=O (carbonyl) groups [60]. The peaks at 1642 $cm^{-1}$ and 690 $cm^{-1}$ are attributed to C=C stretching and bending of alkene, respectively. The peak at 1450 $cm^{-1}$ is due to C-H bending for methyl deformation, while the peak at 1372 $cm^{-1}$ is due to C-O stretching vibration. The important peaks of P-LENR due to epoxy linkages are located at 1241 and 880 $cm^{-1}$. These peaks correspond to the symmetric

and asymmetric stretching vibration of the epoxide ring, respectively [60]. Upon exposing the LENR to the light source without the presence of a catalyst, it can be seen that the spectra Figure 7b show similar peaks with the P-LENR. However, a slight decrease in the intensity was observed in the crucial peaks located at 1241 and 897 $cm^{-1}$ and some shifts were observed to the higher wavenumber when compared to the P-LENR. This indicated that slight degradation of LENR degradation might have occurred [61]. Figure 7c shows the spectra of degraded LENR in the presence of the $Cu^{2+}$-HNT catalyst. A significant decrease in the intensity of the important peaks of LENR was observed, and a peak shifted to 908 $cm^{-1}$ for the asymmetric stretching of the epoxide ring is seen. Subsequently, Figure 7d and 7e show the FT-IR spectra of degraded LENR treated with CuO-HNT calcined at 550 and 900 °C, respectively. As can be seen from the spectra, there is a shift in the crucial peak of LENR to higher wavenumber in spectra of LENR treated with calcined CuO-HNT at 550 °C. Fig. 7d shows better degradation when compared with the spectra of degraded LENR treated with calcined CuO-HNT at 900 °C Figure 7e. This is because there is a more obvious decrease in the epoxy peak originally at 868 $cm^{-1}$ for the catalyst calcined at 550 °C compared to that calcined at 900 °C Furthermore, the peak at 1241 $cm^{-1}$ diminished in the spectra of degraded LENR treated with CuO-HNT calcined at 550 °C whereas it only decreased in intensity in the case of LENR treated with calcined CuO-HNT at 900 °C. This might be due to the distortion of catalyst morphology when calcined at higher temperature which reduces its degradation ability. In all the treated samples, as the intensity of the epoxy peaks decreases, and also increase in the intensity of the absorption peak on all degraded LENR at around 1714 -1716 $cm^{-1}$ (b-e) which is assigned to C=O (carbonyl) groups of aldehyde and ketone, respectively [60]. This is assigned to the ketone which is usually formed due to the chain scission (breaking) in the degraded LENR and an increase in the intensity of the O-H peak were observed. This might be due to partial cleavage of oxirane bonds of degraded LENR that were converted to the terminal diols and carbonyl compounds as reported by [25]. Generally, when compared between P-LENR and all degraded LENR, a decrease in the intensity of peak at 690 $cm^{-1}$ (a-e) allocated to (-C=C- bending) for alkene indicates the consumption of double bond during degradation process [62][63].

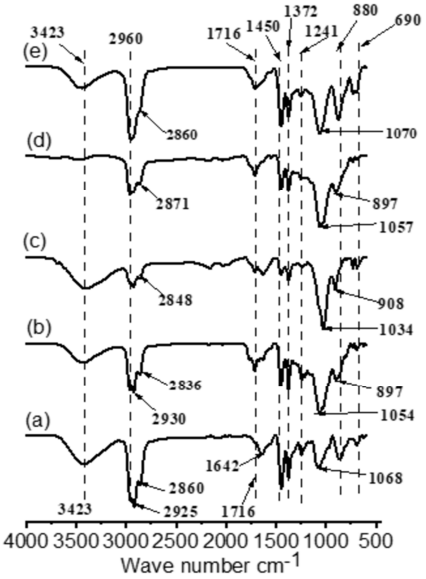


**Fig. 7:** FT-IR Spectra of (a) P-LENR, (b) D-LENR without catalyst, (c) D-LENR with 0.05g $Cu^{2+}$-HNT, (d) D-LENR with 0.05g Calcined CuO-HNT at 550 °C, (e) D-LENR with 0.05g Calcined CuO-HNT at 900 °C.

### 3.7.3 Thermogravimetric analysis (TGA)

Figures 8 (i) and 8 (ii) shows the TGA and derivative thermogravimetry (DTG) plots of P-LENR and photodegraded LENR treated with 0.05 g catalysts assigned as (a, b, c, d, and e). Their $T_{onset}$, $T_{max}$ and $T_{offset}$ are summarized in the Table 3. Thermograms of TGA and DTG reveals that the degradation of P-LENR occurred in three stages. As can be seen in Figure 8(i) the thermogram showed a slight weight loss between 31 – 150 °C due to the evaporation of moisture or solvent in the LENR. This causes 5.6 % weight loss. The second stage of degradation started at 211°C and ends at 273 °C with a $T_{max}$ of 238 °C. This weight loss is due to the degradation of oligomers and volatile materials [61]. Beyond 273 °C the weight loss is approximately 89% and correspond to the degradation of high $M_w$ LENR.

Generally, weight loss and shift in the peaks positions was observed for all photodegraded LENR

in comparison to P-LENR. However, the degraded LENR generally showed two different profiles depending on the catalysts used to degrade the LENR. The first profile (peak) is slightly like that of P-LENR. This can be seen for the degraded LENR obtained without any catalyst and with the CuO-HNT calcined at 900 °C catalyst. For both these two samples, the profiles exhibited a high % of weight loss at high temperatures of above 275 °C, like the P-LENR. This indicates that even after the degradation process, a large portion of the sample still existed as high $M_w$ LENR. In contrast, the degraded LENR using the $Cu^{2+}$-HNT and CuO-HNT calcined at 550 °C catalysts showed lower % of weight loss at temperatures above 275 °C. As such, this may indicate that for both these catalysts, a higher portion of the LENR is degraded to lower $M_w$ LENR. Subsequently, it can be observed that for all the degraded LENR, the $T_{max}$ for the weight loss at above 275 °C is more or less like P-LENR. All samples exhibit a $T_{max}$ in the range of 407 – 416 °C. Interestingly, for the degraded LENR using the $Cu^{2+}$-HNT and CuO-HNT calcined at 550 °C catalysts, there seems a large shift in the $T_{max}$ to lower temperatures than 275 °C when compared to P-LENR. This can be due to the availability of lower $M_w$ LENR as compared to the P-LENR and other degraded LENR. As can be seen that both P-LENR and degraded LENR samples when heated above 600 °C, their percentage residue approached zero except the degraded LENR treated with $Cu^{2+}$-HNT. This might be due to some amount of catalyst still remaining in the degraded LENR sample.

**Table 3**
TGA of P-LENR and degraded LENR

| Samples | $T_{onset}$ (°C) | $T_{max}$ (°C) | $T_{end}$ (°C) | % Residue at 600 °C |
|---|---|---|---|---|
| P-LENR (a) | 292.11 | 418.97 | 418.97 | 2 |
| D-LENR (no catalyst) (b) | 305.94 | 407.86 | 407.86 | 5 |
| D-LENR treated with 0.05g $Cu^{2+}$-HNT (c) | 268.08 | 416.95 | 416.95 | 25 |
| D-LENR treated with 0.05g calcined CuO-HNT at 550 °C (d) | 285 | 412.96 | 412.96 | 4 |
| D-LENR treated with 0.05g calcined CuO-HNT at 900 °C (e) | 298 | 414.87 | 414.87 | 0 |

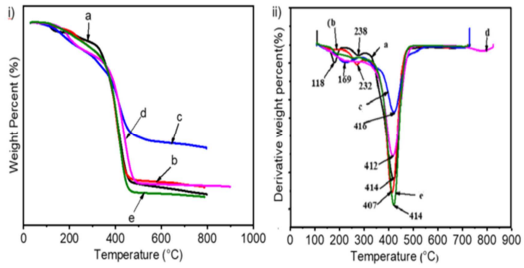


**Fig. 8:** (i) and (ii)showed TGA and DTG spectra of (a) P-LENR and degraded LENR b) with no catalyst (c) treated with 0.05 g $Cu^{2+}$-HNT (d) treated with 0.05 g calcined CuO-HNT at 550 °C and (e) treated with 0.05 g Calcined CuO-HNT at 900 °C.

## 4. Conclusions

Cu was successfully immobilized onto HNT by impregnation technique, and some portion of the resulting nanocomposite was subjected to calcination at 550 and 900 °C respectively to obtain calcined CuO-HNT nanocomposite. Both as-synthesized and calcined nanocomposites were characterized via FTIR, UV-Vis (DRS), PL, XRD, SEM/EDX, $N_2$ - adsorption desorption and AAS. The results indicate successful formation of un-calcined and calcined nano catalyst. The findings showed that the sample calcined at 550 °C has less agglomeration compared to that calcined at 900 °C. The BET surface area also drastically reduced for samples calcined at 900 °C. The catalytic activity of the as-synthesized and calcined catalysts was assessed for the degradation of LENR using UV-irradiation photocatalytic method in the presence of a UV light. The degree of degradation was assessed by comparing the changes in $M_w$ between P-LENR and the degraded samples. The

decrease in $M_w$ was observed for various photodegraded samples compared to P-LENR. The LENR ($M_w$ = 25,732 g/mol) degraded to 12,067 g/mol, without catalyst, while with uncalcined catalyst $Cu^{2+}$-HNT $M_w$ is 5,774 g/mol, calcined CuO-HNT at 550 °C $M_w$ is 3,105 g/mol, and calcined CuO-HNT at 900 °C $M_w$ is 8,078 g/mol. The result reveals that the LENR degraded in the presence of calcined CuO-HNT catalyst at 550 °C has lower molecular weight which indicates that it has higher catalytic activity over the remaining catalyst samples. This study has shown that the presence of $Cu^{2+}$-HNT, and CuO-HNT nanocomposites under UV light enhances the degradation of LENR and may find useful application as a potential source for renewable fuel and fine chemicals. Optimization of various reaction parameters would be interesting route to investigate to improve the catalytic reaction.

## 5. Acknowledgements

We would like to acknowledge the grant received from University Research Grant, Universiti Sains Malaysia 1001/PKIMIA/8011071, which supported this work.

## 6. Conflicts of Interest

There are no conflicts to declare.

## 7. References

[1] Sabeeh, M., Liaquat, R. and Maryam, A. Effect of alkaline and alkaline-photocatalytic pretreatment on characteristics and biogas production of rice straw. *Bioresource Technology,* 309, 123449 (2020). doi.org/10.1016/j.biortech.2020.123449

[2] Ebrahiem E. E., Hakim Y. A., Aboul-Fotouh T. M., and Elfattah M. A., "Improvement of diesel fuel to enhance engine performance and emissions using zinc oxide nanoparticle additive," *Egyptian Journal of Chemistry*, 65(2), 349–355(2022), doi: 10.21608/EJCHEM.2021.87012.4206.

[3] Liu C., Wu S., Zhang H., and Xiao R., "Catalytic oxidation of lignin to valuable biomass-based platform chemicals: A review," *Fuel Process. Technology*, 191, 181–201(2019), doi: 10.1016/j.fuproc.2019.04.007.

[4] Toor S. S., Rosendahl L., and Rudolf A., "Hydrothermal liquefaction of biomass: A review of subcritical water technologies," *Energy*, 36(5), 2328–2342(2011),doi: 10.1016/j.energy.2011.03. 013.

[5] Kambo H.S., Minaret J. and Dutta A. Process water from the hydrothermal carbonization of biomass: a waste or a valuable product. *Waste and Biomass Valorization*, *9*(7),1181-1189(2018).doi: 10.1007/s12649-017-9914-0.

[6] Wang C., Zhu C., Huang J., Li L., and Jin H., "Enhancement of depolymerization slag gasification in supercritical water and its gasification performance in fluidized bed reactor," *Renewable. Energy*, 168, 829–837(2021), doi: 10.1016/j.renene.2020.12.104.

[7] Zhang S., Dong Q., Zhang L., and Xiong Y., "High quality syngas production from microwave pyrolysis of rice husk with char-supported metallic catalysts," *Bioresource Technology*, 191, 17–23, (2015), doi: 10.1016/j.biortech.2015.04.114.

[8] Li C., Zhao X., Wang A., Huber G. W., and Zhang T., "Catalytic Transformation of Lignin for the Production of Chemicals and Fuels," *Chemical Review.* 115(21), 11559–11624(2015), doi:10. 1021/acs.chemrev.5b00155.

[9] Chio C., Sain M., and Qin W., "Lignin utilization: A review of lignin depolymerization from various aspects," *Renewable Sustainable Energy Review*, 107, 232–249(2019), doi: 10.1016/j.rser.2019.03. 008.

[10] Ma J., Shi S., Jia X., Xia F., Ma H., Gao J. and Xu J., Advances in catalytic conversion of lignocellulose to chemicals and liquid fuels. *Journal of Energy Chemistry*, *36*, 74-86(2019), https://doi.org/10.1016/j. jechem.2019.04.026

[11] Liu X., Duan X., Wei W., Wang S., and Ni B.J., Photocatalytic conversion of lignocellulosic biomass to valuable products. *Green Chemistry*, *21*(16), 4266-4289(2019), https://doi.org/10.1039/C9GC01728C.

[12] Akram N., Guo J., Ma W., Guo Y., Hassan A., and Wang J., "Synergistic Catalysis of $Co(OH)_2$/CuO for the Degradation of Organic Pollutant Under Visible Light Irradiation," *Scientific Report*, 10(1), 1–12(2020), doi: 10.1038/s41598-020-59053-9.

[13] Samir M., Salah D., Donia S., and Kasry A., "Effect of Surface Chemical Modification on the Self Assembly of Metal Nanoparticles," *Egyptian Journal of Chemistry*, 65(1), 685–689(2022), doi: 10.21608/EJCHEM.2021.85558.4160.

[14] Massaro M., Colletti C.G., Lazzara, G., Milioto S., Noto, R., and Riela S. Halloysite nanotubes as support for metal-based catalysts. *Journal of Materials Chemistry*

*A*, *5*(26), 13276-13293(2017). doi: 10.1039/c7ta02996a.

[15] Yaqoob A.A., Parveen T., Umar K. and Mohamad I.M.N., Role of nanomaterials in the treatment of wastewater: a review. *Water*, *12*(2), 495(2020), doi:10.3390/w12020495

[16] Jawaid M., Ahmad A., Ismail N. and Rafatullah M., *Environmental Remediation Through Carbon Based Nano Composites*. *Green Energy and Technology* Springer.2021.https://link.springer. com/book/10.1007/978-981-15-6699-8

[17] Lim H.H., Chua P.N., Mun H.P., Horri B.A. and Salamatinia, B., Synthesis, and characterisation of CuO/HNT nanoparticles through in-situ glycine nitrate process. *International Journal of Advances in Science Engineering and Technology*, *6*(2), (2019).

[18] Prashar S., Hor M., Díaz-s M., and Lama M., "Applied Clay Science Multifunctional catalysts based on palladium nanoparticles supported on functionalized halloysites: Applications in catalytic C-C coupling , selective oxidation and dehalogenation reactions," 214, (2021), doi: 10.1016/j.clay.2021.106272.

[19] Cavallaro G., Lazzara G., Milioto S., and Parisi F., "Hydrophobically Modified Halloysite Nanotubes as Reverse Micelles for Water-in-Oil Emulsion," *Langmuir*, 31(27), 7472–7478, (2015), doi: 10.1021/acs.langmuir.5b01181.

[20] Zhang Y., He X., Ouyang J., and Yang H., "Palladium nanoparticles deposited on silanized halloysite nanotubes: Synthesis, characterization and enhanced catalytic property," *Scienfic Report*, 3(29), 1–6(2013), doi: 10.1038/srep02948.

[21] Koe W.S., Lee J.W., Chong W.C., Pang Y.L. and Sim L.C., An overview of photocatalytic degradation: photocatalysts, mechanisms, and development of photocatalytic membrane. *Environmental Science and Pollution Research*, *27*(3), 2522-2565(2020), https://doi. org/10.1007/s11356-019-07193-5.

[22] Carrillo A.M. and Carriazo J.G. Cu and Co oxides supported on halloysite for the total oxidation of toluene. *Applied Catalysis B: Environmental*, *164*, 443-452(2015). doi:10.1016/j.apcatb.2014.09.027.

[23] Lisuzzo, L., Cavallaro, G., Milioto, S. and Lazzara, G., Halloysite nanotubes as nanoreactors for heterogeneous micellar catalysis. *Journal of Colloid and Interface Science*, *608*, 424-434(2022), doi: 10.1016/j.jcis.2021.09.146.

[24] Azhar N.H.A., Jamaluddin N., Md Rasid H., Mohd Yusof M.J. and Yusoff S.F.M. Studies on hydrogenation of liquid natural rubber using diimide. *International Journal of Polymer Science*, *2015*, 2015.doi: 10.1155/2015/243038.

[25] Rooshenass P., Yahya R. and Gan S.N. Comparison of three different degradation methods to produce liquid epoxidized natural rubber. *Rubber Chemistry and Technology*, *89*(1),177-198(2016).doi:10.5254/RCT.15.84878.

[26] Rooshenass P., Yahya R., and Gan S.N., Preparation of liquid epoxidized natural rubber by oxidative degradations using periodic acid, potassium permanganate and UV-irradiation. *Journal of Polymers and the Environment*, *26*(4), 1378-1392(2018) doi:10. 1007/s10924-017-1038-x.

[27] Guda V.K. and Toghiani H. Catalytic pyrolysis of pinewood using metal oxide catalysts in an integrated reactor system. *Biofuels*, *8*(5),527-536(2017). doi:10.1080/17597269.2016.1231960.

[28] Ibrahim S., Daik R., and Abdullah I. Functionalization of liquid natural rubber via oxidative degradation of natural rubber. *Polymers*, *6*(12),2928-2941(2014).doi: 10.3390/polym6122928.

[29] Bahruddin I. Fadhillah Septian, A. Wiranata and Zahrina I. "Molecular Weight of Liquid Natural Rubber (LNR) Product from the Chemical Depolymerization Process of High Molecular Weight Narutal Rubber Latex," *Journal of Physics: Conference Series.*1655(1) 012091 (2020), doi: 10.1088/1742-6596/1655/1/012091.

[30] Ibrahim S., Othman N., Sreekantan S., Tan, Nor Z. M., and Ismail H., "Preparation and characterization of low-molecular-weight natural rubber latex via photodegradation catalyzed by nano $TiO_2$," *Polymers (Basel).* 10(11),(2018), doi: 10.3390/polym10111216.

[31] Zango Z.U., Abu Bakar N.H.H., Tan W.L. and Bakar M.A. Enhanced removal efficiency of methyl red via the modification of halloysite nanotubes by copper oxide. *Journal of Dispersion Science and Technology*, *39*(1), 148-154(2018) https://doi.org/10.1080/01932691.2017.1301259

[32] Zango Z.U., Garba Z.N., Bakar N.A., Tan W.L. and Bakar M.A. Adsorption studies of $Cu^{2+}$–Hal nanocomposites for the removal of 2, 4, 6-trichlorophenol. *Applied Clay Science*, *132*,68-78(2016).doi: 10.1016/j.clay.2016.05.016.

[33] Allalou S., Kheribet R., and Benmounah A. Effects of calcined halloysite nano-clay on the mechanical properties and microstructure of low-clinker cement mortar. *Case Studies in Construction Materials*, *10*,00213(2019).doi: 10.1016/j.cscm. 2018.e00213.

[34] Turek A., Wieczorek K. and Wolf W.M. Digestion procedure and determination of heavy metals in sewage sludge—An analytical problem. *Sustainability*, *11*(6),4–10,(2019).doi: 10.3390/su11061753.

[35] Phinyocheep P., Phetphaisit C.W., Derouet D., Campistron I., and Brosse J.C. Chemical degradation of epoxidized natural rubber using periodic acid: Preparation of epoxidized liquid natural rubber. *Journal of applied polymer science*, *95*(1),6-15(2005).doi:10.1002/app. 20812.

[36] Kadir H.A., Bakar N.A., Sabri N.A., Abdullah F.H., Bakar M.A., Furuno H. and Saito N. Silver nanoparticles incorporated in dicarboxylic/TEPA modified halloysite nanotubes for the degradation of organic contaminants. *Applied Surface Science*, *531*, p.147417(2020), doi: 10.1016/j. apsusc.2020.147417.

[37] Aytekin M.T. and Hoşgün H.L. Characterization studies of heat-treated halloysite nanotubes. *Chemical Papers*, *74*(12), 4547-4557(2020).doi:10.1007/s11696-020-01263-6.

[38] Yang Y., Xu D., Wu Q., and Diao P. $Cu_2O$/CuO bilayered composite as a high-efficiency photocathode for photoelectrochemical hydrogen evolution reaction. *Scientific reports*, *6*(1),1-13,(2016).doi: 10.1038/srep35158.

[39] Yaqoob A.A., Ibrahim M.N.M., Yaakop A.S., Umar K. and Ahmad A., Modified graphene oxide anode: A bioinspired waste material for bioremediation of Pb2+ with energy generation through microbial fuel cells. *Chemical Engineering Journal*, *417*, 128052 (2021). doi: 10.1016/j.cej.2020.128052.

[40] Lun H., Ouyang J. and Yang H. Natural halloysite nanotubes modified as an aspirin carrier. *RSC advances*, *4*(83),44197-44202(2014).doi: 10.1039/c4ra09006c.

[41] Yu D., Wang J., Hu W., and Guo R., "Preparation and controlled release behavior of halloysite/2-mercapto benzothiazole nanocomposite with calcined halloysite as nanocontainer," *Material. Design.*,129,103–110(2017),doi: 10.1016/j. matdes.2017.05.033.

[42] Jinhua W., Xiang Z., Bing Z., Yafei Z., Rui Z., Jindun L. and Rongfeng C. Rapid adsorption of Cr(Vi) on modified halloysite nanotubes. *Desalination*, *259*(1-3),22-28(2010).doi: 10.1016/j.desal.2010.04.046.

[43] Yuan P., Tan D., Annabi-Bergaya F., Yan W., Liu D., and Liu Z. From platy kaolinite to aluminosilicate nanoroll via one-step delamination of kaolinite: effect of the temperature of intercalation. *Applied, Clay Science*, *83*,68-76(2013).doi: 10.1016/j.clay.2015.05.001.

[44] Hussain S.K., Nagaraju G., Pavitra E., Raju, G.S.R. and Yu J.S. $La(OH)_3$: $Eu^{3+}$ and $La_2O_3$: $Eu^{3+}$ nanorod bundles: growth mechanism and luminescence properties. *CrystEngComm*, *17*(48), 9431-9442 (2015).doi: 10.1039/c5ce01688f.

[45] Aghazadeh M., Golikand A.N., Ghaemi M. and Yousefi T. $La_2O_3$ nanoplates prepared by heat-treatment of electrochemically grown La $(OH)_3$ nanocapsules from nitrate medium. *Journal of the Electrochemical Society*, *158*(12),136,(2011).doi: 10.1149/2.057112jes.

[46] Pezeshkpour S., Salamatinia B. and Horri B.A. Synthesis and characterization of nanocrystalline NiO-GDC via sodium alginate-mediated ionic sol-gel method. *Ceramics International*, *44*(3), 3201-3210,(2018).doi: 10.1016/j.ceramint.2017.11.091.

[47] Huang Z., Lin Q., Luo H., Guo P., Weng, Q., Lei, Y., Cheng, S. and Liu, S.S. Degradation of progesterone by coexisting free radical and nonradical pathways in the CuO/HNTs-PS system. *Chemical Engineering Journal*, *398*, 125458(2020).doi: 10.1016/j.cej.2020.125458.

[48] Cheng Z.L. and Sun W. Preparation of nano-CuO-loaded halloysitenanotubes with high catalytic activity for selective oxidation of cyclohexene. *Chinese Chemical Letters*, *27*(1),81-84(2016).doi: 10.1016/j.cclet.2015.08.002.

[49] Karickhoff B. G. W., and Wkarickhoff S., "Optical absortion spectral a of clay minerals," *Clays Clay Minerals.*, 21(1),59–70(1973).

[50] Molaei A., Amadeh A., Yari M. and Afshar M.R. Structure, apatite inducing ability, and corrosion behavior of chitosan/halloysite nanotube coatings prepared by electrophoretic deposition on titanium substrate. *Materials Science and Engineering:C*, *59*,740-747(2016).doi:10.1016/j.msec.2015.10. 073.

[51] Murali D.S., Kumar S., Choudhary R.J., Wadikar A.D., Jain M.K. and Subrahmanyam A. Synthesis of $Cu_2O$ from CuO thin films: Optical and electricalproperties. *AIP advances*, *5*(4),16(2015), doi: 10.1063/1.4919323.

[52] Deshpande M.P., Patel K.N., Gujarati V.P., Patel K., and Chaki S.H. Structural, thermal, and optical properties of nickel oxide (NiO) nanoparticles synthesized by chemical precipitation method. In *Advanced Materials Research* 1141,65-

71(2016).doi:10.4028/www.scientific.net/amr.1141.65.

[53] Ali, W., Ullah, H., Zada, A., Alamgir, M.K., Muhammad, W., Ahmad, M.J. and Nadhman, A. Effect of calcination temperature on the photoactivities of ZnO/SnO2 nanocomposites for the degradation of methyl orange. *Materials Chemistry and Physics*, *213*, 259-266 (2018). doi.org/10.1016/j.matchemphys.2018.04.015

[54] Talib N.N.A., Bakar N.H.H.A., Bakar M.A., Iqbal A. and Yusof N.H. Depolymerisation of liquid epoxidized natural rubber (LENR) using lanthanum hydroxide ($La(OH)_3$)-HNT Catalyst. In *IOP Conference Series: Materials Science and Engineering* 509(1)012104(2019).doi: 10.1088/1757-899X/509/1/012104.

[55] Huang C.Y., Chatterjee A., Liu S.B., Wu S.Y. and Cheng C.L. Photoluminescence properties of a single tapered CuO nanowire. *Applied surface science*, *256*(11),3688-3692(2010).doi: 10.1016/j.apsusc.2010.01.007.

[56] Horti N.C., Kamatagi M.D. and Nataraj S.K. Photoluminescence properties of copper oxide nanoparticles: Effect of solvents. In *AIP Conference Proceedings*, 2100(1),2-7,(2019).doi: 10.1063/1.5098602.

[57] Zhang, W., Yan, X. and Du, C. Halloysite nanotubes supported copper oxide composites used as efficient catalysts for bisphenol A removal. *Applied Clay Science*, *224*,106509 (2022). doi.org/10.1016/j.clay.2022.106509

[58] Derikvandi, H. and Nezamzadeh-Ejhieh, A. Increased photocatalytic activity of NiO and ZnO in photodegradation of a model drug aqueous solution: effect of coupling, supporting, particles size and calcination temperature. *Journal of hazardous materials*, *321*, 629-638, (2017). doi.org/10.1016/j.jhazmat.2016.09.056.

[59] Parra, M.R. and Haque, F.Z. Aqueous chemical route synthesis and the effect of calcination temperature on the structural and optical properties of ZnO nanoparticles. *Journal of Materials Research and Technology*, *3*(4), 363-369 (2014) doi.org/10.1016/j.jmrt.2014.07.001

[60] Yusof N.H., Darji D., Mohd Rasdi F.R. and Baratha Nesan K.V. Preparation and characterisation of liquid epoxidised natural rubber in latex stage by chemical degradation. *Journal of Rubber Research*, *24*(1), 93-106(2021). doi.org/10. 1007/s42464-02000076
-2

[61] Tahir N.A.M., Azhar N.H.A., Rasidi H.M. and Yusoff S.F.M. Penghidrogenan getah asli cecair dan getah asli cecair terepoksida menggunakan diimida. *Journal of Polymer Science and Technology*, *2*(1), 1-10(2017).doi: 10.17576/mjas-2017-2106-20.

[62] Azhar N.H.A., Rasid H.M. and Yusoff S.F.M. Chemical modifications of liquid natural rubber. In *AIP Conference Proceedings* 1784(1), 1-7, (2016). doi: 10.1063/1.4966762.

[63] Abdullahi S.S., Abu Bakar N.H.H. and Yusof N.H. Facile synthesis of nickel-based supported halloysite nanotube catalysts and their role in photocatalytic degradation of liquid epoxidized natural rubber. *Iranian Polymer Journal*, **32**, 337–351 (2023). doi: https://doi.org/10.1007/s13726-022-01127-8